AAS 23-155

SPACECRAFT PASSIVE SAFETY ASSESSMENT USING ELLIPSE CONSTRAINTS AND RELATIVE ORBITAL ELEMENTS

Bruce Barbour[*], Matthew I. Hunter[†], Riley Fitzgerald [‡], Matthew A. Vavrina [§], David E. Gaylor [¶]

This paper presents necessary and sufficient conditions for validating spacecraft passive safety using relative orbital elements (ROE) centered around the far-field to near-field trajectory design of a hypothetical autonomous rendezvous and docking (AR&D) mission. The specific formulation of the ROEs used in this study are of quasi-nonsingular form based on relative eccentricity/inclination vectors. Current methodologies for ensuring passive safety apply keep-out volumes (KOV) to maintain appropriate separation between the Servicer and Client. Widely used techniques to assess the integrity of the KOV involve forward propagation of the relative Cartesian state to check for a potential KOV breach. In this study, an alternative approach to the propagation-based method is proposed using ROEs due to their valuable geometric insights of spacecraft relative motion. Modeling the relative trajectory and KOV ellipsoids as ellipses into the 2-D ROE sub-space simplifies the passive safety validation to a root-finding problem within the unit disk with high computational efficiency. Other approaches to intersection detection of the KOV are also evaluated in accuracy and run-time. Furthermore, a Monte Carlo simulation was employed to compare the ROE-based and relative Cartesian approaches in terms of maneuver error.

INTRODUCTION

Advancements in computer technology, heightening demand of space exploration, and diminishing launch costs create the framework for new opportunities in autonomous rendezvous and docking (AR&D) mission design. Within the past half century, the concept of rendezvous and docking was largely in the realm of crewed space missions, where a highly skilled astronaut used visual cues and manual piloting to approach and dock with a second spacecraft.[1] The first mission that applied successful docking of two spacecraft occurred on March 16, 1966, during the Gemini 8 mission. NASA astronauts Neil A. Armstrong and David A. Scott accomplished this significant achievement that later spun into the success of the Apollo program. A year after Gemini 8, the first fully automated docking mission was successfully achieved by the Soviet space program. This mission was carried out by Kosmos 186 and 188 through the Soviet Igla system using radar telemetry.[2]

Current spacecraft missions that rely heavily on AR&D capabilities include the SpaceX Dragon crew vehicle[3] and Boeing CST-100 Starliner[3] for approach and docking with the International Space Station (ISS); NASA's Orion spacecraft for Lunar Gateway rendezvous and docking;[4] and many other missions with contemporary focus on the ISS. However, NASA has recently pushed for new heights in mission design that employs the use of AR&D for in-space servicing, assembly, and manufacturing (ISAM) technologies. Although in-space servicing of satellites has been observed in past missions such as the Mission Extension Vehicle (MEV)[5] and Orbital Express,[6] the On-orbit Servicing, Assembly, and Manufacturing 1 (OSAM-1) will become one of the first semi-autonomous space missions to perform on-orbit refueling and assembly.[7]

[*]Ph.D. Candidate, Aerospace and Ocean Engineering, Virginia Tech, Blacksburg, VA 24060.
[†]Ph.D. Candidate, Aeronautical and Astronautical Engineering, Stanford University, Stanford, CA, 94305.
[‡]Assistant Professor, Aerospace and Ocean Engineering, Virginia Tech, Blacksburg, VA 24060.
[§]Senior Systems Engineer, a.i. solutions, Lanham, MD, 20706.
[¶]Aerospace Engineer, NASA Goddard Space Flight Center, Greenbelt, MD 20771.

The mission may have significant ramifications in reduced space mission costs, increased spacecraft lifespan, and greater flexibility of on-orbit construction.

Executing a successful autonomous rendezvous will require careful planning to reduce the risk of collision. Current efforts in minimizing this risk make use of passively safe trajectories in the far- and near-field, such as co-elliptic orbits and a walking safety ellipse (WSE).[8] Spacecraft safety is accomplished through the use of 3-D regions centered on the Client called keep-out volumes (KOV), also known as keep-out zones (KOZ), for ensuring a safe approach of the Client. The dimensions of the KOVs are defined by a variety of factors, including expected navigational uncertainty which improves within each ensuing sub-phase of the trajectory.[7]

Passive safety evaluations in far- and near-field trajectories utilize the KOVs as a baseline to prevent breaching of unauthorized zones. Reference 7 defines passive safety as unforced motion that maintains the integrity of the KOV. Specific to the mission design in OSAM-1, a time factor is also involved for remaining outside of the driving KOV if it refrains from executing a propulsive maneuver for 24 hours following an abort.[7]

Modeling and tracking the relative dynamics for assessing passive safety is typically conducted in the Radial, In-Track, and Cross-Track (RIC) reference frame. Addressing the problem of passive safety validation can also be accomplished through the application of quasi-nonsingular relative orbital elements (ROE). Early concepts of ROEs utilized relative eccentricity/inclination (E/I) vector separation through the works of D'Amico.[9] Recent space missions, including GRACE,[10] TanDEM-X/TerraSAR-X,[11] and PRISMA[12] have employed the E/I separation concept for guaranteeing minimum range separation from the target spacecraft. In a similar fashion, ROEs can be used in the context of AR&D passive safety checks adhering to the integrity of KOVs.

In contrast to the ROE application of guidance problems,[13] this study focuses on developing a technique of validating passive safety of unforced spacecraft motion using ROEs. Common methods for checking for passive safety utilize numerical propagation of the relative spacecraft state to actively evaluate potential breach of the KOV in the RIC frame. Using the ROE formulations that describe ellipse characteristics of a projected RC-plane relative orbit from Sullivan[14] and an efficient method to find conic intersection points from Fitzgerald,[15] an ROE-based Passive Safety technique is proposed in this study that complements the current propagation-based methods. ROEs are advantageous for passive safety analysis in that they can easily model a 2-D projected relative orbit as a closed ellipse, enabling root solver methods to determine KOV intersections. This approach exploits a one-dimensional, complex polynomial for fast computational time in solving for these intersections,[15] which initial simulations demonstrate promising results. This expected outcome is an ROE-based validation method for AR&D passive safety that is comparable in accuracy to numerical propagation methods but has the potential for significantly less computational resources and simplifies the relative motion model in the context of E/I separation.

TRAJECTORY OVERVIEW

This section introduces the reference frames implemented in the trajectory design as well as provides a general description of a hypothetical AR&D trajectory for a non-cooperative Client that will be used extensively in the analysis. Client is capitalized throughout this paper to differentiate from the Servicer spacecraft. The trajectory is based on the NASA OSAM-1 mission design.[7] It also presents a brief summary on strategies planned to be used by NASA for maintaining passively safe rendezvous. The last subsection provides some discussion on the simulation setup with various techniques used to model and propagate the spacecraft.

Relative Cartesian System

Much of the trajectory design utilizes the RIC frame, which is a local relative Cartesian frame centered about the Client. Using this reference frame provides simpler modeling of the dynamics because the axes are more aligned with the principal directions of motion compared to other systems. Its $\hat{e}_R$-axis is its radial vector that points from the center of the primary body to the Client, $\hat{e}_C$-axis is coincident with the orbital angular momentum vector, and $\hat{e}_I$-axis is the vector normal to the $\hat{e}_R$- and $\hat{e}_C$-axes, completing the right-handed triad; best highlighted in Figure 1.

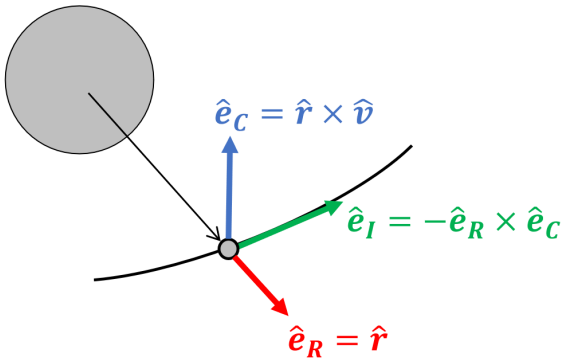

Figure 1: Representation of the RIC Cartesian reference frame.

The RIC frame can also be represented using Spherical coordinates, offering a valuable approach for modeling thrust vectors in a 3-D space by separating their magnitude and direction. In this representation, δr represents the relative radial distance from the Client to the Servicer, θ denotes the angle measured within the orbital plane of the Client, and ϕ signifies the angle measured from the Client's orbital plane to the position vector of the Servicer. To aid in visualization, Figure 2 provides an illustration of this reference frame.

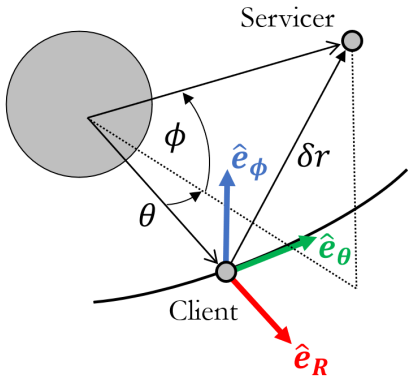

Figure 2: Representation of the RIC Spherical reference frame.

Passively Safe Trajectories

Although passive safety defined in Reference 8 includes the 24-hour window following an abort, this study focuses on the KOV as the driving factor of achieving passive safety in each of the trajectory segments highlighted in Table 1. For the scope of this study, the hypothetical trajectory design has been intentionally developed to be passively safe. Therefore, each segment of the rendezvous trajectory (and its subsequent transfer trajectory) will naturally maintain the integrity of its associated driving KOV. Figures 3 and 4 are generated plots from *FreeFlyer*[16] that provide the visual of the trajectory.

To maintain passive safety with the Client, the rendezvous trajectory utilizes co-elliptic orbits and a WSE to achieve closer proximity to the Client just before the V-bar approach for capture. In the literature, common techniques to approach a spacecraft during proximity operations are known as V-bar (in-line with the flight path of the Client) and R-bar (perpendicular to the flight path along line of radius vector of the Client).[17] Although the R-bar approach is not used in this rendezvous concept, the trajectory design incorporates passing the R-bar with minimum safe radial separation to achieve required in-track separation "ahead" of the Client.

A co-elliptic orbit is useful in the far-field trajectory due to nearly constant separation of the aligned radius vectors between the Servicer and Client. This orbit configuration is defined by parallel positioning of the line

Table 1: Absolute orbital elements of the Client and Servicer through each segment of the trajectory design.

Designated Orbit	a (km)	e	i (deg)	ω (deg)	Ω (deg)
Client	7.2000e3	1.0000e-5	9.7900e1	9.3202e1	1.0330e2
Servicer Co-Elliptic 0	7.1950e3	1.0001e-5	9.7900e1	9.3202e1	1.0330e2
Servicer Co-Elliptic 1	7.2167e3	1.5778e-3	9.7890e1	1.0925e2	1.0338e2
Servicer Co-Elliptic 2	7.2059e3	2.2269e-3	9.7896e1	7.0970e1	1.0375e2
Servicer Walking Safety Ellipse	7.2061e3	1.3716e-3	9.7897e1	5.5887e1	1.0399e2

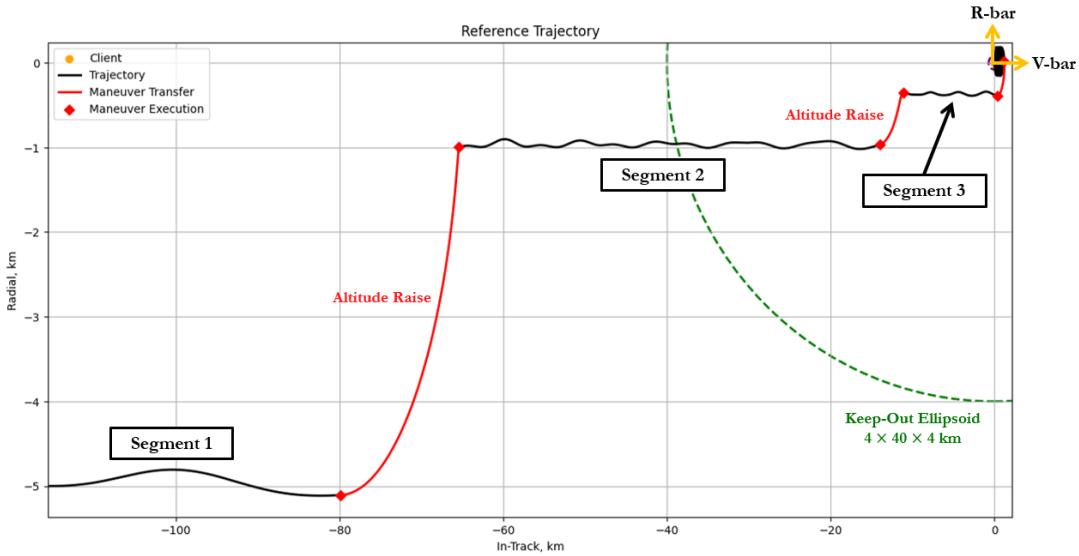

Figure 3: Reference passively safe AR&D trajectory (projected in RI-plane).

of apsides between the two spacecraft, enabling the radial separation to be equivalent at the apses.[7] Three different co-elliptic orbits are used throughout the AR&D trajectory with lowering of radial separation of 5 km, 1 km, and 0.350 km for each proceeding orbital raise transfers as presented in Table 1, respectively. Transferring between co-elliptic orbits is achieved through pairs of orbital raise and stop maneuvers using an impulsive burn assumption. It is assumed that the Client does not perform any translational maneuvers throughout the rendezvous trajectory.

Once the Servicer coasts beyond the R-bar at the third co-elliptic orbit, the spacecraft will perform a maneuver to transfer and insert into a carefully designed WSE. Table 1 provides the absolute orbital elements of the servicing spacecraft for the WSE at the point of insertion. WSE is an inherently-safe trajectory that is effective at minimizing the risk of the spacecraft crossing the V-bar while preserving the integrity of the KOV. The hypothetical KOV dimensions are described in Table 2 for the outer keep-out ellipsoid, middle keep-out ellipsoid, and inner keep-out sphere; taken from Reference 7. Appropriate phasing of the spacecraft's in-plane and out-of-plane motion ensures minimum range separation along radial and cross-track while safeguarding a constant in-track drift rate. Figures 4 and 5 illustrate the projected motion of the WSE of the reference trajectory in the RI- and RC-plane, respectively, where the WSE does not breach the KOV at any point. Once

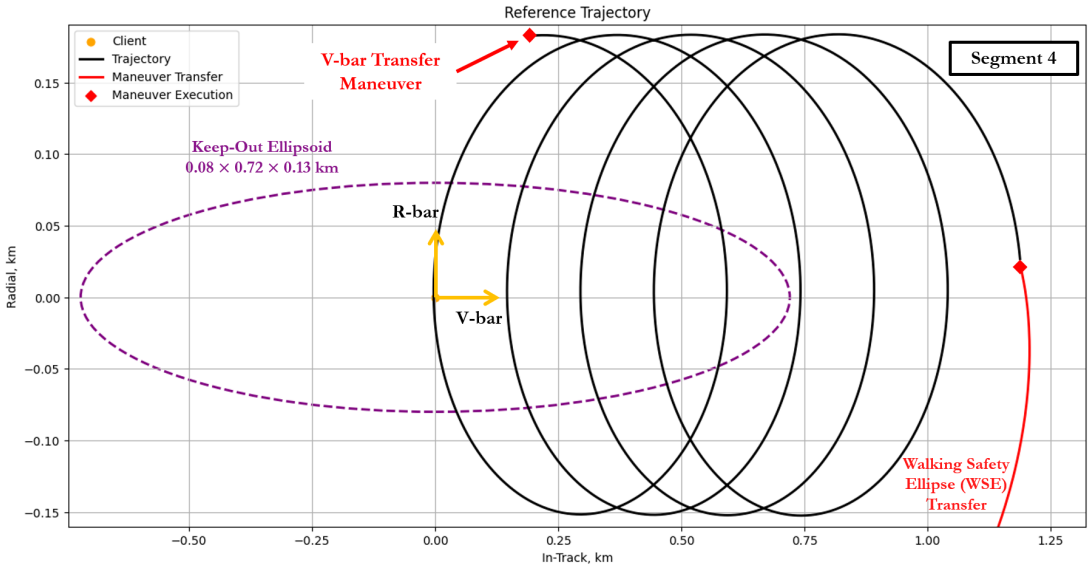

Figure 4: Walking Safety Ellipse (WSE) of the reference passively safe AR&D trajectory (projected in RI-plane).

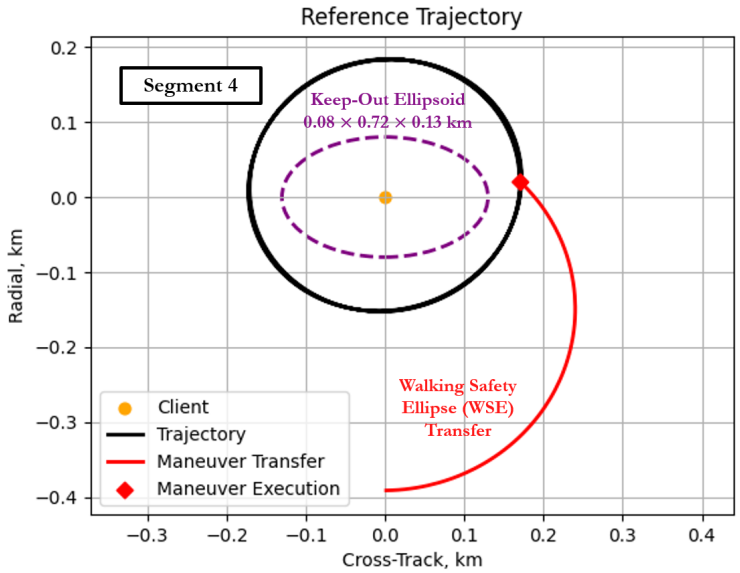

Figure 5: Walking Safety Ellipse (WSE) of the reference passively safe AR&D trajectory (projected in RC-plane).

the Servicer reaches the quarter mark of its fifth revolution during the WSE (as labeled in Figure 4), the V-bar transfer is executed to commence proximity operations. At this stage, the spacecraft is no longer passively safe and enters an active abort mode with maneuvers required to avoid collision.[7]

Table 2: Dimensions of hypothetical keep-out volumes in RIC frame.

Keep-Out Volume Type	Radial (in km)	In-Track (in km)	Cross-Track (in km)
Outer Keep-Out Volume	4.000	40.00	4.000
Middle Keep-Out Volume	0.080	0.720	0.130

RELATIVE ORBITAL ELEMENTS

The quasi-nonsingular ROEs presented by D'Amico provide geometric insights on the relative orbit model.[9] Figure 6 demonstrates that the defining features of a relative orbit in the RIC frame can be characterized by the ROE state.

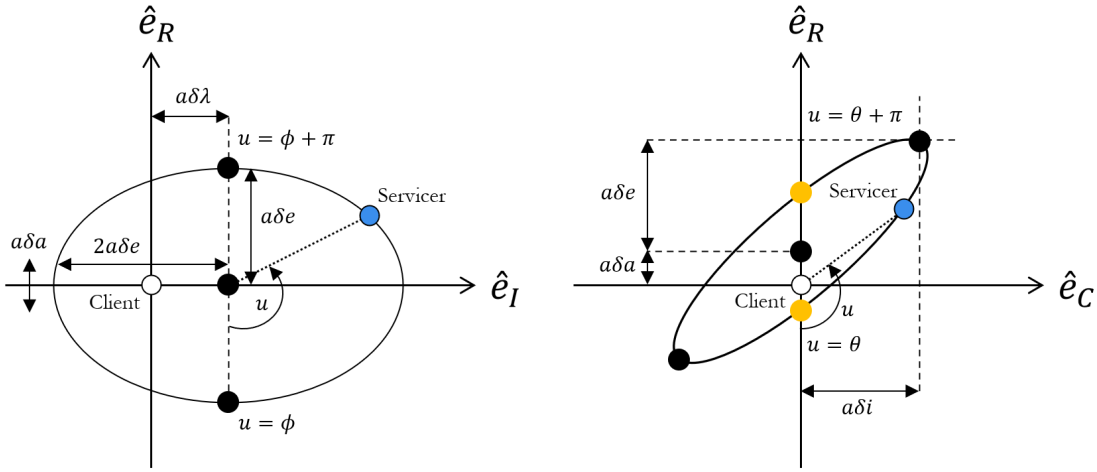

Figure 6: Representation of two arbitrary relative orbits defined by ROEs modeled in the RI-plane and RC-plane (valid for near-circular orbits).

It is worth mentioning that the 2-D projected planes presented in Figure 6 do not represent the same relative orbit as they have differing radial separation. A nonzero radial separation affects the RI-plane by introducing in-track drift, but this does not have the same effect in the RC-plane which maintains its closed shape. ROEs are also not limited to describing relative orbits that exhibit an elliptical shape. This specific formulation of ROEs can be applied to virtually all forms of relative motion in a Client-Servicer model (also known as Chief/Deputy) and is not subject to linearization errors. As expressed in Eq. (1), the osculating ROEs are functions of the osculating Keplerian elements of the Servicer and Client.[9]

$$\delta\vec{\alpha} = \begin{bmatrix} \delta a \\ \delta\lambda \\ \delta e_x \\ \delta e_y \\ \delta i_x \\ \delta i_y \end{bmatrix} = \begin{bmatrix} (a_s - a_c)/a_c \\ (M_s - M_c) + (\omega_s - \omega_c) + (\Omega_s - \Omega_c)\cos i_c \\ e_s \cos\omega_s - e_c \cos\omega_c \\ e_s \sin\omega_s - e_c \sin\omega_c \\ i_s - i_c \\ (\Omega_s - \Omega_c)\sin i_c \end{bmatrix} \tag{1}$$

The subscripts s and c reference the Servicer and Client, respectively. In addition, the variables a, e, i, ω, and Ω are five of the six standard Keplerian elements with M as the mean anomaly. ROEs expressed in

this form are dimensionless quantities but when multiplied by semi-major axis (SMA) of the Client provide physical dimensions to the relative motion model as shown in Figure 6. The in-plane quantities δa and $\delta\lambda$ are relative semi-major axis and relative mean longitude, respectively. In addition, the remaining four elements are components of the in-plane relative eccentricity vector $\delta\vec{e}$ and out-of-plane relative inclination vector $\delta\vec{i}$.

Mapping from ROEs to the Cartesian coordinate system is possible through a first-order equivalence between ROEs and the integration constants of the Hill-Wiltshire-Clohessy (HCW) equations.[9] This yields a state-transition matrix (STM) in the ROE frame that is almost equivalent to the relative Cartesian frame. Since the ROEs are derived from the absolute orbital elements, the resulting relative Cartesian state $\delta\vec{x}^{\mathcal{R}}$ accurately describes the motion of the relative spacecraft dynamics in a near-circular orbit. Eq. (2) is the Lyapunov transformation $P(t)$ that supplies the direct mapping.[14]

$$\delta\vec{x}^{\mathcal{R}} \approx a_c \begin{bmatrix} 1 & 0 & -\cos u_c & -\sin u_c & 0 & 0 \\ 0 & 1 & 2\sin u_c & -2\cos u_c & 0 & 0 \\ 0 & 0 & 0 & 0 & \sin u_c & \cos u_c \\ 0 & 0 & n_c \sin u_c & -n_c \cos u_c & 0 & 0 \\ 0 & 0 & 2n_c \cos u_c & 2n_c \sin u_c & 0 & 0 \\ 0 & 0 & 0 & 0 & n_c \cos u_c & n_c \sin u_c \end{bmatrix} \delta\vec{\alpha} = P(t)\delta\vec{\alpha} \tag{2}$$

The variables n and $u(t) = M(t) + \omega$ denote the mean motion and mean argument of longitude, respectively. Taking the inverse of the transformation matrix will reattain the ROE state. However, it is not recommended to map from the relative Cartesian system to the ROEs when using the HCW STM for propagation due to associated linearization errors.

According to Chernick, the ROEs can be plotted in the following phase-space trajectories: (δa, $\delta\lambda$), (δe_x, δe_y), and (δi_x, δi_y).[18] These plots entail the relative dynamics referenced about the center of the relative orbit rather than the spacecraft as seen in the RIC frame. Using these phase-space trajectories simplifies the spacecraft motion significantly. As shown in Figure 7, a general WSE in the RIC frame has elliptical motion in the RC-plane but forms a helix-like shape in the RI-plane. The yellow circle represents the Client, whereas the blue circle represents the Servicer.

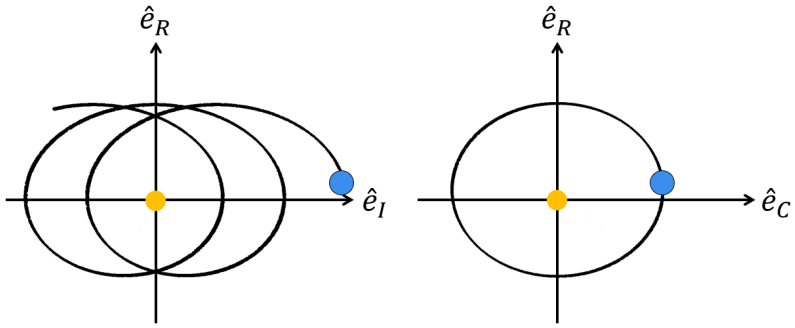

Figure 7: Illustration of the general walking safety ellipse (WSE) in the two-body problem (2BP) expressed in the RIC frame.

On the contrary, using the ROE phase-space trajectories shown in Figure 8 simplifies the representation of the relative motion to linear and constant states. Maximizing separation between the two spacecraft in the RC-plane can be achieved through parallel or anti-parallel alignment of the relative eccentricity/inclination vectors.[9] This can be easily tracked through phase-space trajectories in (δe_x, δe_y) and (δi_x, δi_y) where the phasing of the vectors is $\phi = atan2(y, x)$. For a WSE, the phases of the relative eccentricity/inclination vectors are identical.[18]

The phase-space trajectories in (δa, $\delta\lambda$) compared to its RI-plane counterpart exhibits nearly 1-D motion. Since the spacecraft is modeled based on its relative orbit center, the sinusoidal behavior observed in $\hat{e}_R$ of

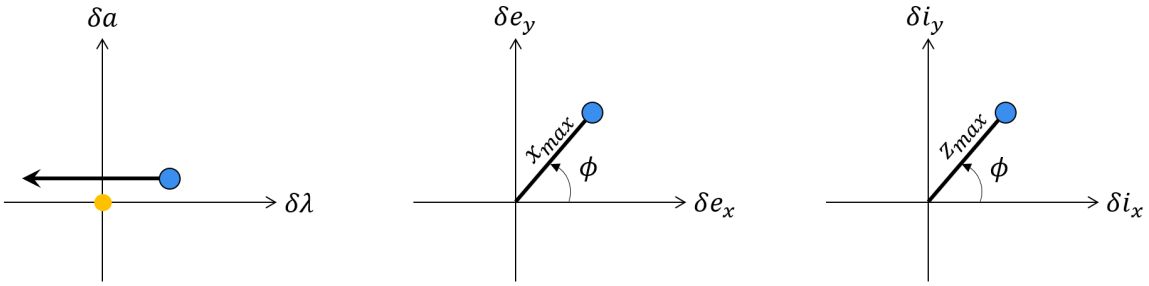

Figure 8: Illustration of the general WSE in the 2BP expressed in the ROE phase-space trajectories.

the Cartesian system reduces to a constant. Though, periodic gravitational perturbations can be expected to induce slight oscillation in the (δa, $\delta\lambda$) trajectory. Mitigating the effects of perturbations on the ROE phase-space (specifically within short-time periods) can be accomplished by converting the osculating ROEs to the mean ROEs using the Brouwer transformation.[19] However, observing the effects of mean ROEs falls beyond the scope of this study.

METHODOLOGY

This section derives the necessary and sufficient conditions to ensure passive safety in RC using the ROE state. It is assumed that the ROEs used in these analyses describe an osculating orbit. In the first subsection, spatial conditions of the projected relative motion in the RC-plane are derived and provided as mathematical inequalities. This derivation will help explain the origin and utilization of the Polynomial Conic Intersection (PCI) test, which aids in evaluating relative motion for potential KOV breach. A special case of the PCI test, referred to as PCI-Simplified or PCIS, will also be derived to reduce computational complexity while preserving accuracy. Additionally, a discussion on the analysis of passive safety for post-maneuver trajectories with variable thrust vectors will be presented.

ROE-based Passive Safety

As relative motion can vary in behavior, this study focuses on developing three conditions defined in ROEs to guarantee passive safety. These conditions exploit the linear mapping of ROEs to the relative Cartesian state, as described in Eq. (2). Each of the three conditions are bolded for readability.

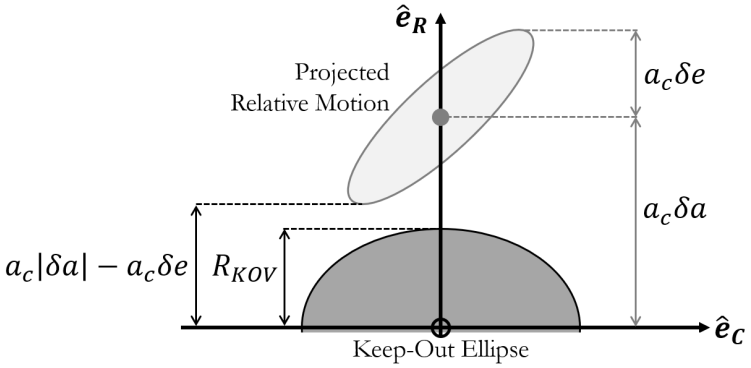

Figure 9: Projected elliptical relative orbit in the RC-plane illustrating the radial buffer condition.

The first condition is simply a radial buffer where the minimum separation in the $\hat{e}_R$ direction of the RC-plane projected ellipse satisfies the integrity of the semi-minor axis of the keep-out ellipse. This can

be checked by finding the lowest point along the projected relative motion, and ensuring that the $\hat{e}_R$ value of this point is outside of the keep-out ellipse. This is a necessary and sufficient condition as formulated in Eq. (3).

$$a_c|\delta a| - a_c\delta e > R_{KOV} \tag{3}$$

The variable a_c denotes the Client' SMA and R_{KOV} is the radius of the KOV in the direction $\hat{e}_R$. As illustrated in Figure 9, as long as no portion of the projected relative motion crosses the R_{KOV} line, the spacecraft is determined to be passively safe. Although not shown, C_{KOV} is the KOV radius in the cross-track direction. This equation is applicable to relative orbits residing above or below the keep-out region. It is worth noting that such a condition can also be applied to nearly all relative orbit types. However, in some cases, the radial buffer condition may be violated but the relative motion is still considered passively safe.

If the relative motion of the servicing spacecraft does not satisfy the radial buffer condition, then the last two conditions mentioned can be evaluated. These conditions ensure that the orbit of the Servicer does not intersect the driving KOV nor lies completely within the KOV by taking advantage of the ellipse characteristics of the projected relative motion. Evaluating these conditions require that these ellipse characteristics be defined by the ROE state. Therefore, the semi-major and semi-minor axes of the projected relative orbit in the RC-plane can be determined using a singular value decomposition (SVD) of the Lyapunov transformation that maps the ROE state to the relative Cartesian frame.[14]

$$\overline{\sigma}_{RC} = \frac{a_c}{\sqrt{2}}\left[\delta e^2 + \delta i^2 + \sqrt{\delta e^4 + \delta i^4 - 2\delta e^2\delta i^2\cos\left(2(\phi-\theta)\right)}\right]^{1/2} \tag{4}$$

$$\underline{\sigma}_{RC} = \frac{a_c}{\sqrt{2}}\left[\delta e^2 + \delta i^2 - \sqrt{\delta e^4 + \delta i^4 - 2\delta e^2\delta i^2\cos\left(2(\phi-\theta)\right)}\right]^{1/2} \tag{5}$$

$$\psi = \frac{1}{2}\arctan\left(2\delta e\delta i\sin\left(\phi-\theta\right), \delta e^2 - \delta i^2\right) \tag{6}$$

These quantities are represented as $\overline{\sigma}_{RC}$ for the semi-major axis, $\underline{\sigma}_{RC}$ for the semi-minor axis, and ψ as the tilt angle measured from $\hat{e}_C$. As shown in Eqs. (4)-(6), these are functions of the ROE state and Client's SMA. The variables ϕ and θ are the phase angles of the relative eccentricity and inclination vectors measured from the x-component, respectively. **To satisfy the first of the two ellipse-based conditions, $\overline{\sigma}_{RC}$ and $\underline{\sigma}_{RC}$ must be larger than their safety ellipse counterparts as shown in Eq. (7).** This is generalized using the maximum and minimum of the two KOV radii to correspond with the semi-major and semi-minor axes of the projected RC-plane ellipse of the relative orbit, respectively.

$$\begin{cases} \overline{\sigma}_{RC} > \max(R_{KOV}, C_{KOV}) \\ \underline{\sigma}_{RC} > \min(R_{KOV}, C_{KOV}) \end{cases} \tag{7}$$

Once it has been determined that the relative orbit's projected RC-plane ellipse has dimensions larger than that of the KOV, then the projected ellipse must be evaluated for intersection points with the KOV. There are many methods to check for ellipse intersections, which this study analyzes several as detailed in the next section. *All three conditions need not be met to guarantee passive safety;* one condition (radial buffer) is necessary and sufficient to guarantee passive safety. The two remaining conditions are codependent, in other words, both must be true to guarantee passive safety. Additionally, it can be easily understood that checking for the radial buffer condition is less numerically intensive compared to the ellipse-based conditions. Therefore, it is most efficient to check for the radial buffer before tackling the ellipse problem. Figure 10 provides an algorithm that implements this approach.

Deriving the Projected RC-Plane Ellipse

To evaluate the intersection of the projected RC-plane ellipses of the KOV and relative trajectory, it is necessary to express both ellipses as equations. Using the general equation of a rotated and translated ellipse

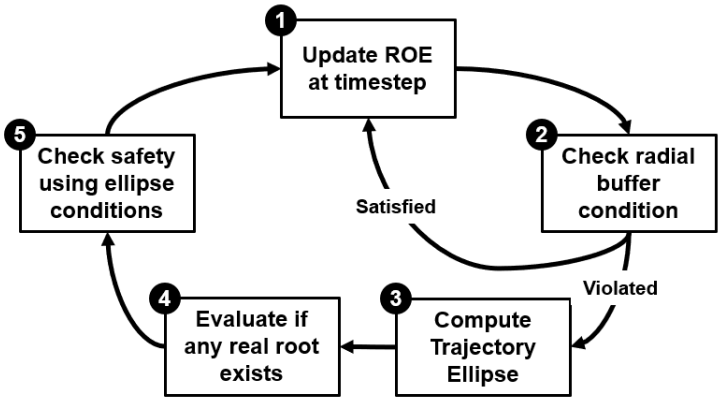

Figure 10: High-level algorithm flowchart for determining ROE-based Passive Safety.

provided in Eq. (8), the two ellipses can be formulated using each of their individual parameters.

$$\frac{((x-h)\cos(\chi)+(y-k)\sin(\chi))^2}{\alpha^2}+\frac{((x-h)\sin(\chi)-(y-k)\cos(\chi))^2}{\beta^2}=1 \tag{8}$$

Since the origin of the RIC frame most commonly represents the Client, the KOV can be expressed as the standard ellipse equation that omits rotation and translation. On the other hand, the relative trajectory projected in the RC-plane does not have orbit-centered cross-track separation from the origin as illustrated in Figure 6. Therefore, the ellipse equation can be simplified to only having translation in the radial direction, i.e., the variable h reduces to zero. Here k is the orbit-centered radial separation, χ is the ellipse tilt angle measured from $\hat{C}$, α is the ellipse semi-major axis, and β is the ellipse semi-minor axis. For the KOV, the quantities h, k, and χ are zero, reducing it to the common standard ellipse equation. Eq. (8) can be rewritten in a polynomial form, making it more refined to easily identify the polynomial coefficients.

$$c_5x^2+c_4xy+c_3y^2+c_2x+c_1y+c_0=0 \tag{9}$$

These coefficients in Eq. (9) are functions of the ellipse quantities k, χ, α, and β, which are provided below.

$$c_5=\frac{\cos^2(\chi)}{\alpha^2}+\frac{\sin^2(\chi)}{\beta^2} \tag{10}$$

$$c_4=\frac{\sin(2\chi)}{\alpha^2}-\frac{\sin(2\chi)}{\beta^2} \tag{11}$$

$$c_3=\frac{\sin^2(\chi)}{\alpha^2}+\frac{\cos^2(\chi)}{\beta^2} \tag{12}$$

$$c_2=\frac{k\sin(2\chi)}{\beta^2}-\frac{k\sin(2\chi)}{\alpha^2} \tag{13}$$

$$c_1=\frac{-2k\sin^2(\chi)}{\alpha^2}-\frac{2k\cos^2(\chi)}{\beta^2} \tag{14}$$

$$c_0=-1+\frac{k^2\sin^2(\chi)}{\alpha^2}+\frac{k^2\cos^2(\chi)}{\beta^2} \tag{15}$$

Polynomial Conic Intersection (PCI) Test

Within mathematical literature, numerous methods exist to identify intersection points between two ellipses. One particularly effective technique is the novel Polynomial Conic Intersection (PCI) test developed by Fitzgerald,[15] which offers a straightforward yet computationally efficient approach to finding intersections between any two non-degenerate conics. We can express Eq. (9) in its matrix quadratic form,

$$\begin{bmatrix} x & y & 1 \end{bmatrix} \begin{bmatrix} a_i & {}^{b_i}\!/_2 & {}^{d_i}\!/_2 \\ {}^{b_i}\!/_2 & c_i & {}^{e_i}\!/_2 \\ {}^{d_i}\!/_2 & {}^{e_i}\!/_2 & f_i \end{bmatrix} \begin{bmatrix} x \\ y \\ 1 \end{bmatrix} = \boldsymbol{N}^{\mathsf{T}} \boldsymbol{M}_i \, \boldsymbol{N} = \boldsymbol{0} \tag{16}$$

The unit circle, given by the equation $x^2 + y^2 = 1$, can be represented in a similar form using the coefficient matrix $\boldsymbol{M}_C = \mathrm{diag}(1, 1, -1)$. Suppose that an ellipse defined by $\boldsymbol{N}^{\mathsf{T}} \boldsymbol{M}_1 \, \boldsymbol{N} = \boldsymbol{0}$ is a transformed image of the unit circle expressed as $\boldsymbol{N'}^{\mathsf{T}} \boldsymbol{M}_C \, \boldsymbol{N'} = \boldsymbol{0}$. The coordinate systems of the ellipse and the unit circle are connected through a linear transformation, where $\boldsymbol{N} = \boldsymbol{W}_1 \boldsymbol{N'}$; thus,

$$\boldsymbol{N}^{\mathsf{T}} \boldsymbol{M}_1 \boldsymbol{N} = \boldsymbol{N'}^{\mathsf{T}} \boldsymbol{W}_1^{\mathsf{T}} \boldsymbol{M}_C \boldsymbol{W}_1 \boldsymbol{N'} \tag{17}$$

Assuming the existence of the ellipse ($\boldsymbol{M}_1$ is neither positive-definite nor negative-definite) and considering it to be non-degenerate or non-singular, we proceed with the understanding that $\boldsymbol{M}_1$ is symmetric. By performing the eigen-decomposition of $\boldsymbol{M}_1$ as $\boldsymbol{M}_1 = \boldsymbol{V}_1 \, \boldsymbol{\Lambda}_1 \, \boldsymbol{V}_1^{\mathsf{T}}$, we can propose (without loss of generality) that the eigenvalues are ordered in Λ_1 according to the sign pattern $(+, +, -)$, such that $\lambda_1 > \lambda_2 > 0 > \lambda_3$. It is worth mentioning that since $\boldsymbol{M}_1$ and $-\boldsymbol{M}_1$ define the same ellipse, we can negate all eigenvalues if two negative λ_i exist.

We can redefine the eigenvalue matrix $\boldsymbol{\Lambda}_i = \boldsymbol{L} \, \boldsymbol{M}_C \, \boldsymbol{L}$ through the diagonal matrix $\boldsymbol{L}$ that contains the ordered square root of the eigenvalues of $\boldsymbol{M}_1$,

$$\boldsymbol{L} = \mathrm{diag}\Big(\sqrt{\lambda_1}, \sqrt{\lambda_2}, \sqrt{-\lambda_3}\Big) \tag{18}$$

and substituting the redefined $\boldsymbol{\Lambda}_i$ with the eigen-decomposition of $\boldsymbol{M}_1$ further expands Eq. (17) to yield,

$$\boldsymbol{N}^{\mathsf{T}} \boldsymbol{M}_1 \, \boldsymbol{N} = \boldsymbol{N'}^{\mathsf{T}} \, \boldsymbol{W}_1^{\mathsf{T}} \, \boldsymbol{V}_1 \, (\boldsymbol{L} \, \boldsymbol{M}_C \, \boldsymbol{L}) \boldsymbol{V}_1^{\mathsf{T}} \, \boldsymbol{W}_1 \boldsymbol{N'} = \boldsymbol{N'}^{\mathsf{T}} \boldsymbol{M}_C \, \boldsymbol{N'} \tag{19}$$

Eq. (19) can be easily rearranged to show

$$\boldsymbol{N}^{\mathsf{T}} \boldsymbol{M}_1 \, \boldsymbol{N} = \boldsymbol{N'}^{\mathsf{T}} (\boldsymbol{L} \boldsymbol{V}_1^{\mathsf{T}} \boldsymbol{W}_1)^{\mathsf{T}} \, \boldsymbol{M}_C (\boldsymbol{L} \boldsymbol{V}_1^{\mathsf{T}} \boldsymbol{W}_1) \boldsymbol{N'} = \boldsymbol{N'}^{\mathsf{T}} \boldsymbol{M}_C \, \boldsymbol{N'} \tag{20}$$

that the ellipse is equivalent to the unit circle in coordinates $\boldsymbol{N'}$ if the parenthetic quantity $(\boldsymbol{L} \boldsymbol{V}_1^{\mathsf{T}} \boldsymbol{W}_1)$ is the identity matrix. This can be accomplished by computing the inverse of $\boldsymbol{V}_1 \boldsymbol{L}^{-1}$ for the relationship $\boldsymbol{L} \boldsymbol{V}_1^{\mathsf{T}} \boldsymbol{W}_1 = \mathbb{I}$. As a result, the mapping $\boldsymbol{W}_1$ becomes a function of the eigenvalues and eigenvectors of $\boldsymbol{M}_1$.

$$\boldsymbol{W}_1 = \boldsymbol{V}_1 \boldsymbol{L}^{-1} = \boldsymbol{V}_1 \mathrm{diag}\Big(\sqrt{\lambda_1}, \sqrt{\lambda_2}, \sqrt{-\lambda_3}\Big) \tag{21}$$

By transforming the coefficient matrix $\boldsymbol{M}_2$ of the second ellipse into these coordinates, we obtain the coefficient matrix $\boldsymbol{H}$. This new matrix represents the ellipse that can be examined for intersections with the unit circle. This approach enables us to solve the original intersection problem effectively.

$$\boldsymbol{H} = \boldsymbol{W}_1^{\mathsf{T}} \boldsymbol{M}_2 \boldsymbol{W}_1 = \begin{bmatrix} a & {}^{b}\!/_2 & {}^{d}\!/_2 \\ {}^{b}\!/_2 & c & {}^{e}\!/_2 \\ {}^{d}\!/_2 & {}^{e}\!/_2 & f \end{bmatrix} \tag{22}$$

With the sufficient coordinate transformation, the coefficients of the complex polynomial $p(z)$ can be computed using the coefficient matrix $\boldsymbol{H}$

$$p(z) = (d + ei)z^3 + 2(a + c + 2f)z^2 + 3(d - ei)z + 2(a - c - bi) \tag{23}$$

where the ellipse of interest will not intersect with the unit circle if and only if $p(z)$ has two roots z inside the unit disk, i.e., $|z_k - 1| < 0$. Eq. (23) can be derived by utilizing the standard conic equation presented in Eq. (9) and parameterizing points on the unit circle using their angle θ as $(x, y) = (\cos\theta, \sin\theta)$. After substituting the parameterized quantities into Eq. (9) to produce a Fourier series and then expressing sine and cosine using their complex exponential forms, we obtain the equation

$$\tfrac{1}{2}(a - c - bi)e^{2i\theta} + (d - ei)e^{i\theta} + (a + c + 2f) + (d + ei)e^{-i\theta} + \tfrac{1}{2}(a - c + bi)e^{-2i\theta} = 0,$$

and introducing the complex variable $z = e^{i\theta}$ then multiplying the equation by z^2 to remove negative powers results in the quartic polynomial equation,

$$q(z) = \tfrac{1}{2}(a - c - bi)z^4 + (d - ei)z^3 + (a + c + 2f)z^2 + (d + ei)z + \tfrac{1}{2}(a - c + bi) = 0 \qquad (24)$$

Here $q(z)$ corresponds to the ellipse intersections with the unit circle, with roots on the unit circle represented as $e^{i\theta_k}$ and consequently a root of the Fourier series. The coefficients of $q(z)$ form a conjugate palindrome, indicating self-inversion and symmetry of roots over the unit circle. This test can further be simplified through Cohn's theorem. The theorem states that a self-inversive polynomial has the same number of roots in the unit disk as the reciprocal polynomial of its derivative, which is the complex polynomial $p(z)$.[20] Hence, if $p(z)$ has two zeros inside the unit disk, the ellipse is free from intersections with the unit circle.

PCI Simplified (PCIS) Test

Given the nature of KOVs in this study, a substantial portion of the PCI test can be omitted. This is because the KOV represented as a projected ellipse in the RC-plane only differs from the unit circle by scaling as opposed to translation and rotation. Consequently, the coordinates of the unit circle and the keep-out ellipse coincide with each other. As a result, the coefficient matrix $\boldsymbol{H}$ can be easily computed accordingly.

$$\boldsymbol{H} = \begin{bmatrix} c_5/C_{KOV}^2 & c_4/2R_{KOV}C_{KOV} & c_2/2C_{KOV} \\ c_4/2R_{KOV}C_{KOV} & c_3/R_{KOV}^2 & c_1/2R_{KOV} \\ c_2/2C_{KOV} & c_1/2R_{KOV} & c_0 \end{bmatrix} = \begin{bmatrix} a & b/2 & d/2 \\ b/2 & c & e/2 \\ d/2 & e/2 & f \end{bmatrix} \qquad (25)$$

The quantities represented by c_i, listed in the same order as Eq. (9), correspond to the coefficients of the ellipse that characterizes the relative trajectory of the Servicer when projected in the RC-plane. As previously mentioned, R_{KOV} and C_{KOV} denote the radial and cross-track dimensions of the KOV, respectively. Moving forward, the remaining steps of the PCIS test involve computing the roots of $p(z)$. This novel approach omits the eigen-decomposition method entirely, further reducing computational time.

Alternative Methods for Ellipse Intersection

Alternative methods for determining projected RC-plane ellipse intersection include `sympy.solve()` and `scipy.fsolve()`. These techniques are categorized by the dimension and nature of the problem it can solve:

sympy.solve() (complex, 2-D) Python library function for solving symbolic polynomials algebraically.

scipy.fsolve() (real, 2-D) Numerical solver from the Python library `SciPy` that utilizes a modified mature version of Powell's method to solve for roots of nonlinear equations.

SIMULATION SETUP

This section provides the setup that was used for running the simulation test cases as well as generating their results. The first subsection discusses the specific force model used in *FreeFlyer* to produce the hypothetical trajectory, including the post-maneuver trajectories that will be discussed later in this section. Specifications on the hardware for running the *FreeFlyer* simulation and Python post-processing algorithms are also presented. The last subsections will discuss the test cases developed to validate the novel intersection methods and evaluate performance of the ROE-based Passive Safety technique.

FreeFlyer Setup

This paper leverages the high-fidelity astrodynamics software *FreeFlyer* to conduct simulations of two spacecraft models representing the Client and Servicer. Both models are subject to a force model that incorporates perturbation effects, including zonal harmonics, atmospheric lift and drag, solar radiation pressure, and third-body effects. The specific properties utilized to simulate the force model are documented in Table 3. Given the significance of these perturbation effects, a choice was made to employ the built-in 9th-order Runge-Kutta integrator with a local tolerance of 10^{-15} and a timestep of 0.1 seconds, ensuring high-accuracy in trajectory propagation. The coefficient quantities c_d, c_l, and c_r are the default values in *FreeFlyer*.

Table 3: ForceModel setup in the *FreeFlyer* astrodynamics software.

ForceModel Property	Specifications
Integrator	RK8(9): tol = 10^{-15}, $\Delta t = 0.1\ sec$
Atmospheric Model	MSIS-90, $c_d = 2.2$, $c_l = 1.2$
Solar Radiation Pressure	Spherical, $c_r = 1.4$
Third-Body	Sun, Moon, …
Zonal Harmonic	10×10

Software and Hardware Specifications

After the trajectories were generated in *FreeFlyer*, the Ephemeris files were input into *Visual Studio Code* (Version 1.79) where they were post-processed using the developed Python algorithms that ran on 64-bit Python 3.9. The hardware used to run the simulations and perform post-processing is an HP Laptop with 11th Gen Intel Core i7 Processor (8 cores, 2.50 GHz) and 32 GB RAM.

Analyzing Ellipse Intersection Methods

To evaluate the accuracy and efficiency of the ellipse intersection methods, two different test cases of parametric sweeps that vary the shape, position, and orientation of elliptical trajectories against the Middle Keep-Out Volume (see Table 2) were considered. In the first test case, a parametric sweep was performed on the semi-major and semi-minor axes of the ellipse, as well as the tilt angle. The translation in the $\hat{e}_R$ direction was kept at zero. Specifically, these ellipse quantities were tested in the range of

$$\epsilon_C \leq \overline{\sigma}_{RC} \leq 2C_{KOV}, \quad \epsilon_R \leq \underline{\sigma}_{RC} \leq 2R_{KOV}, \quad 0^\circ \leq \psi \leq 180^\circ$$

with the timestep values prescribed as $\epsilon_C = 0.01$ km, $\epsilon_R = 0.01$ km, and $\epsilon_\psi = 1^\circ$, respectively. This provided a sufficient dataset of elliptical trajectories that encompassed many different configurations of a safety ellipse.

In order to consider a broader range of potential configurations, the second test case concentrated on the translation of the ellipse while maintaining a constant tilt angle. To introduce complexity and minimize runtime for the sweep generation, a fixed orientation of $\psi = 45^\circ$ was selected. In this case, the parametric sweep used the following range of quantities

$$C_{KOV} \leq \overline{\sigma}_{RC} \leq 2C_{KOV}, \quad R_{KOV} \leq \underline{\sigma}_{RC} \leq 2R_{KOV}, \quad -2R_{KOV} \leq a\delta a \leq 2R_{KOV}, \quad \psi = 45^\circ$$

with timestep values defined as $\epsilon_C = 0.01$ km, $\epsilon_R = 0.01$ km, and $\epsilon_{a\delta a} = 0.001$ km, respectively.

Variable Thrust Vectors for Walking Safety Ellipse Insertion

A Monte Carlo simulation with uniform distribution of the thrust vector components was utilized in *FreeFlyer* to explore variations in burn magnitude and direction for the nominal Walking Safety Ellipse Insertion (WSEI) maneuver. The WSEI maneuver, depicted in Figure 4, enables the Servicer to enter a WSE trajectory, ensuring passive safety by maintaining desired radial and cross-track separations with the Client. However, real-world scenarios necessitate accounting for maneuver errors that may result in an unsafe trajectory. To address this, 5000 trials were conducted, modifying the percentage burn magnitude from 0 to 120% and adding noise to the angular directions by -10° to 10°, using the RIC spherical frame of reference (refer to Figure 2).

To assess the passive safety condition of the off-nominal WSE, post-maneuver trajectories were propagated forward in time using the prescribed WSE time-of-flight (TOF) of 7 hours. The evaluation involved verifying that all RC-plane points along the trajectory maintained a safe distance from the driving KOV. Since the keep-out ellipse can be represented as a standard ellipse $f(x, y)$, determining if $f(x, y) \leq 1$ occurs can be easily accomplished. To minimize process time, the trajectory was evaluated per one-tenth orbital revolution. This would yield 17 snapshots of the spacecraft state history per trial, but only the relative states determined to be passively safe were logged with the rest of states omitted (except for the initial unsafe relative state) from the output Ephemeris file. These findings were then compared to the ROE-based Passive Safety technique to showcase its efficacy in detecting unsafe trajectories. However, time dependency in the passive safety evaluation for both the RIC-based and ROE-based techniques was not factored in.

RESULTS & DISCUSSION

This section presents the results of the three analyses conducted to assess the effectiveness of the ROE-based Passive Safety technique. In order to address the complete algorithm, it is critical to have a reliable method for determining a breach in the KOV based on the projected RC-plane ellipse characteristics. Hence, it is necessary to evaluate different methods of ellipse intersection to ensure the algorithm's reliability and accuracy in validating passive safety. Subsequently, the ROE-based technique can be used to evaluate the reference trajectory depicted in Figures 3 and 4. As the trajectory was designed to be passively safe, it serves as the truth model for the passive safety assessment. The final analysis will introduce off-nominal cases to verify the algorithm's ability to handle both safe and unsafe trajectories in comparison to a more conventional technique.

Validating the PCI and PCIS Tests

Solving for intersection points of 2-D polynomials is a numerically difficult problem. Therefore, after systematically evaluating alternative methods (not PCI and PCIS) through extensive sampling and visually inspecting graphs to verify their accuracy, Powell's method implemented in `scipy.fsolve()` was chosen as the most robust and mature method for obtaining closest to the true solutions. Although the solutions may not be truth, they are the considered the most robust. The techniques are compared to the `scipy.fsolve()` function in terms of similarity in differentiating between safe and unsafe elliptical trajectories in the parametric sweep cases.

Therefore, based on the dataset generated from the two test cases, an evaluation of the ellipse intersection methods was implemented in terms of percent difference compared to `scipy.fsolve()` and average runtime. As shown in Table 4, the PCIS and PCI tests using eigenvalues of the companion matrix, implemented through `numpy.roots()`,[21] to solve for $p(z)$ had the best performance in both cases. In Case 1, the PCIS test had the lowest percent difference, nearly identical to *SciPy*. In addition to greater similarity, PCIS executed at half the runtime compared to the PCI test, as expected. When introducing varied ellipse translation in Case 2, both tests had identical but marginally lower performance. Yet, the PCIS test still computed faster at a consistent runtime of 0.15 milliseconds, around 69 times faster than *SciPy*. Surprisingly, the symbolic solver `sympy.solve()` performed slightly worse than the PCI and PCIS methods in Case 1 and performed poorly in Case 2 with incredibly slow runtime. Based on the performance between these two tests, the PCIS test will serve as the basis for assessing ellipse conditions for the remaining two analyses in this section.

Table 4: Results of the parametric sweep analysis for KOV breach detection compared to SciPy.

Ellipse Intersection Methodology	Case 1			Case 2		
	Percent Different from SciPy.fsolve (%)	Average Runtime (s)	Runtime Comment	Percent Different from SciPy.fsolve (%)	Average Runtime (s)	Runtime Comment
Powell's method using SciPy.fsolve		0.01159			0.01034	
Symbolic solver using SymPy.solve	0.30%	1.48812	128x slower	18.02%	20.8960	2021x slower
PCIS Test	0.06%	0.00015	77x faster	8.06%	0.00015	69x faster
PCI Test	0.32%	0.00031	37x faster	8.06%	0.00025	41x faster

Performance of the ROE-based Passive Safety

Table 5 provides the performance results of the full algorithm implemented through Figure 10. The table includes results on runtime, which represents the average time taken to execute the algorithm and generate a result. The total average runtime indicates the cumulative time spent within the entire algorithm per timestep while the ellipse intersection test runtime is time spent evaluating just the ellipse conditions. At each timestep of 10 seconds, the algorithm is executed with the assessment result and runtime recorded.

Using the PCIS test, the ROE-based Passive Safety algorithm successfully determined passive safety for each trajectory segment, which consisted of either a co-elliptic orbit or a WSE. The algorithm achieved perfect accuracy by evaluating both the radial buffer and ellipse conditions. In the case of the first three co-elliptic orbits, the sufficient radial buffer condition was met, eliminating the need to verify the ellipse conditions. As a result, the runtime for the ellipse intersection test was not tabulated. However, due to the nature of the WSE, the radial buffer condition was not applicable, requiring the ellipse-based methods to be tested. The tests for the ellipse conditions yielded a short average runtime of 0.13611 milliseconds. All trajectory segments were evaluated with an average runtime less than 0.2 milliseconds. In addition to the

Table 5: Performance of the ROE-based Passive Safety (using PCIS) algorithm on the reference trajectory.

Segment #	Relative Trajectory Type	Passive Safety Validation Accuracy (%)	Ellipse Intersection Test Runtime (ms)	Total Average Runtime (ms)
1	Co-Elliptic	100.00	-	0.02313
2	Co-Elliptic	100.00	-	0.01409
3	Co-Elliptic	100.00	-	0.01679
4	Walking Safety Ellipse	100.00	0.13611	0.17907

performance evaluation of the algorithm, ROE phase-space trajectories of the WSE are provided to illustrate ROE behavior. Expectations of the ROE quantities in different relative trajectories can be used in extension to the passive safety technique for active trajectory monitoring. In this case, simpler motion of the WSE in the ROE phase-space compared to the RIC frame in Figures 4 and 7 provides valuable insight in the context of E/I separation for maximizing the minimum RC-plane separation. Due to orbital perturbations, the spiral shape in the ADE plane and zig-zag in ADI plane are evident but not significant. They are limited within only a few meters. A red circle on the plot indicates the average for the 7 hour time-of-flight, which the quantities $(\delta e_x, \delta e_y)$ and $(\delta i_x, \delta i_y)$ exhibit nearly identical phase angles, where $\phi - \theta \approx 0$. This is in agreement with the models of the phase-space trajectories for the WSE in Figure 8.

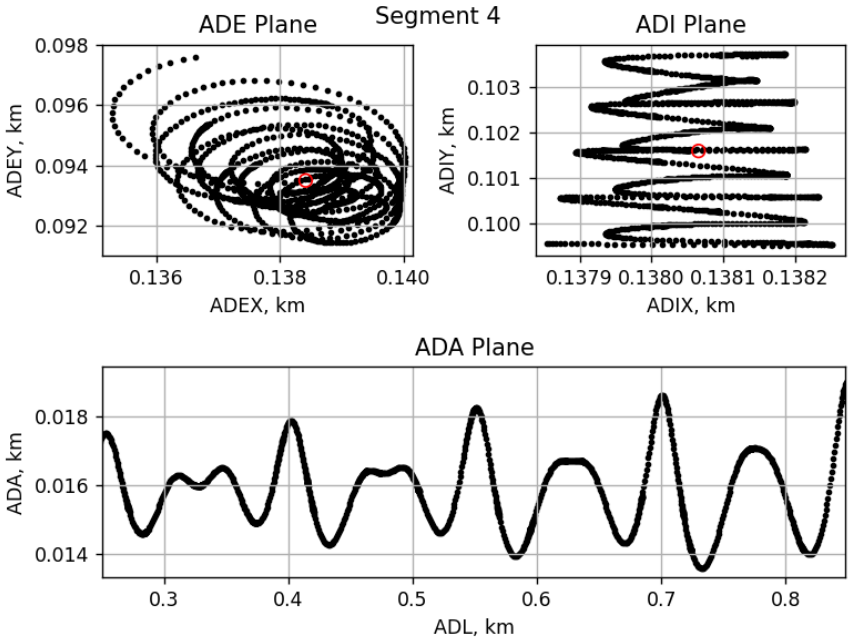

Figure 11: ROE phase-space trajectories for the WSE (segment 4).

Walking Safety Ellipse Insertion Post-Maneuver Error

After the RIC-based Passive Safety evaluation, the Servicer relative state history and its evaluation were post-processed using the ROE-based technique for comparisons. The findings of this analysis are presented in Table 6. Since each Monte Carlo trial had varying number of relative state snapshots as described earlier, the accuracy percentages of the ROE-based technique for overall and safe/unsafe trajectory detection were weighted based on the number of snapshots per trial. As anticipated, the algorithm using the PCIS test demonstrated a consistently low runtime with an average of 0.286 milliseconds. While slightly higher than previous analyses conducted in this study, this difference is considered negligible. In terms of performance, the ROE-based technique was quite good at 96.4% in overall accuracy, with only slightly better performance in detecting unsafe trajectories by around 1%. These results also provide details in the percentage of false-positives and false-negatives. For detecting safe trajectories, the technique was able to capture 96.27% with 3.73% false-negatives. Similarly, the detection of unsafe trajectories yielded 2.72% of false-positives. This performance indicates the the ROE method is highly capable of producing reliable results for assessing post-maneuver passive safety, but improvements can be made to mitigate false results.

Table 6: Performance in post-maneuver passive safety assessment for variable thrust error.

Sample Size	Overall Weighted Accuracy (%)	Weighted Accuracy (safe) (%)	Weighted Accuracy (unsafe) (%)	KOV Breach Test Runtime (ms)		Total Runtime (ms)	
				Mean	SD	Mean	SD
5000	96.404	96.272	97.283	0.23750	0.22507	0.28600	0.27389

Performance of the ROE-based Passive Safety technique can also be viewed in the ROE phase-space. Figures 12 and 13 depict these phase-space trajectories in the $a\delta e$ and $a\delta i$ phase-planes, where each point represents an individual Monte Carlo trial conducted during the analysis. In these figures, the blue-colored

'o' indicates a safe trajectory, while peach-colored 'x' represents an unsafe trajectory. These phase-space plots provide a visual representation of the level of accuracy demonstrated by the ROE method in Table 6. Interestingly, the post-maneuver trajectories from the thrust vector errors resulted in the $a\delta i$ phase-plane to

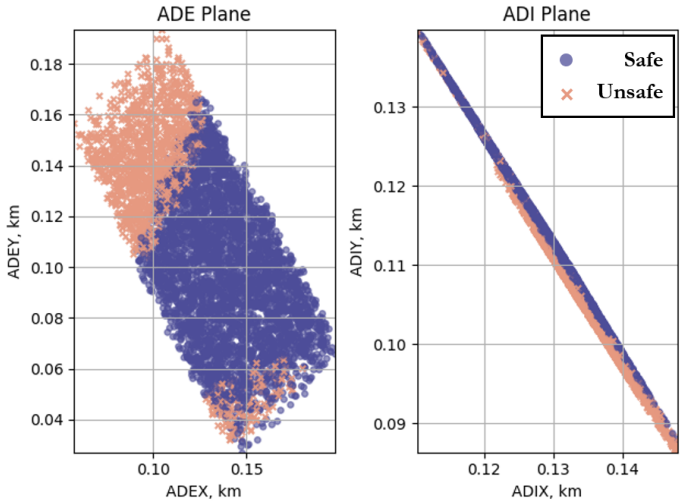

Figure 12: Results of the RIC-based Passive Safety assessment in ADE/ADI planes.

exhibit nearly linear behavior, where changes in the thrust vector maintains the $(\delta i_y/\delta i_x)$ relationship. According to the research findings of D'Amico and Riggi, this linear behavior correlates to the maneuver location defined by the Client's true anomaly (computed from M_c).[22] Reference 24 illustrates that for near-circular orbits, the in-plane and out-of-plane maneuvers expressed in the relative Cartesian are fully decoupled. This results in only out-of-plane maneuvers affecting out-of-plane changes in ROE state, and the same is true for in-plane maneuvers. Since $a\delta i$ is primarily affected by normal maneuvers, the varying thrust direction has the same effect as the varying burn magnitude. Consequently, the decoupling constrains the change in the thrust vector, causing the $a\delta i$ phase-plane to remain close to the observed trajectory.

Among the 3.5% of overall incorrect assessments, a significant fraction is concentrated in the lower-right region of the $a\delta e$ phase-plane near the observed minimum of $a\delta e_y$ of the Monte Carlo simulation. This suggests that there may be limitations to the ROE method when dealing with values within this specific region. One possibility is the effects of zonal harmonics. According to D'Amico, J_2 can cause the $\delta\vec{e}$ to rotate slowly over time, but these effects are often negligible in short-time periods.[9] However, post-maneuver WSE trajectories that are very close to the KOV may cause a breach due to slightly unparalleled motion affecting the calculations of Eqs. (4)-(6). This phenomenon can also be observed in the ADE plane of Figure 11. Therefore, to reduce the effects, the prescribed TOF of the WSE becomes critical. Mean ROEs may be utilized here to further minimize the effects on the calculations of the ellipse characteristics. Additional investigations would provide a better understanding of the precise limitations or potential inaccuracies. Though, the majority of the assessments are consistent with the RIC-based Passive Safety evaluation, indicating a general alignment between the two techniques. It is important to note that although certain trajectories were evaluated to be unsafe, they may still be considered passively safe when introducing a time factor; however, this falls out of scope of this study.

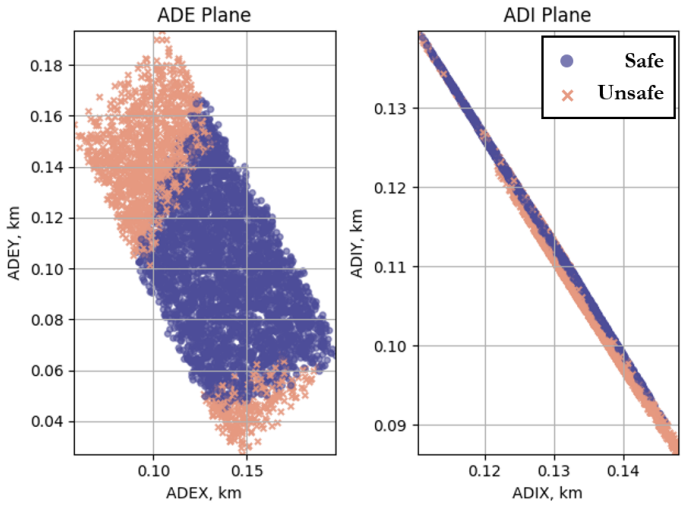

Figure 13: Results of the ROE-based Passive Safety assessment in ADE/ADI planes.

CONCLUSIONS

We have presented a technique used for evaluating passive safety between two spacecraft in a rendezvous trajectory through the application of KOVs and ROEs. The ROE-based Passive Safety technique used the novel PCIS test to assess intersection points between the projected RC-plane ellipses of the KOV and relative orbit. Compared to other intersection methods, the PCIS test was proven to be highly accurate with incredible computational efficiency. When combined with the ROE-based Passive Safety algorithm, preliminary results have demonstrated promising accuracy, at a rate of 100% compared to a reference trajectory and 96.4% overall in post-maneuver trajectory analysis. Additional improvements to the technique can be made to mitigate errors in false-positive (2.72%) and false-negative (3.73%) outputs. ROE phase-space trajectories were also investigated to provide a visual representation of the technique in action, enabling graphical means of identifying safe and unsafe trajectories. The technique developed in this study stands as a promising approach for potential on-board trajectory monitoring systems.

Future works will pursue additional parametric sweep analysis would be beneficial to identify precise limitations. It is speculated that for orbits of high eccentricity may cause the technique to perform poorly due to the specific ROE formulations used. Accounting for eccentricity in the ROEs can be achieved through the modified eccentricity vector developed by Sullivan.[18] Additionally, testing the ellipse conditions can be limited by the ellipse intersection method used. In this study, the Python library *NumPy* was used to determine the roots within the unit disk for the PCIS test, which has been found to have variable performance for repeated roots. One particular method that may improve the accuracy of the KOV breach detection test is the Jenkins-Traub algorithm, a fast and powerful polynomial root-finding technique. Another method is the Lehmur-Shur test that can introduce a more closed form approach. A valuable avenue for further research is the development of a cascading Monte Carlo to simulate off-nominal trajectories from the reference trajectory defined in this paper. Statistical analysis of the results could provide insights into expected ROE behavior and improve the determination of the passive safety condition by employing E/I separation. Machine learning models, such as a Support Vector Machine (SVM), may contribute greater performance. Lastly, replacing the osculating orbital elements with the mean orbital elements to compute the ROE quantities can lessen computational load. The current approach involves computing osculating ROEs at each timestep for the passive safety evaluation. However, the use of mean ROEs per trajectory segment can minimize propagation by achieving convergence of the $a\delta e$ and $a\delta i$ phase-plane trajectories.

ACKNOWLEDGMENTS

The authors of this paper would like to thank the NASA Pathways program for providing the opportunity and facility to conduct this research in supporting NASA's mission. Also, I would like to extend thanks to Dr. Michael Shoemaker, Wayne Yu, and JP Burke for their extremely helpful guidance and constructive feedback.

REFERENCES

[1] K. Mars, *55 Years Ago: Gemini VIII, the First Docking in Space*. Available: www.nasa.gov/feature/55-years-ago-gemini-viii-the-first-docking-in-space: NASA, 2021.

[2] M. Garcia, *50 Years Ago: The First Automatic Docking in Space*. Available: www.nasa.gov/feature/50-years-ago-the-first-automatic-docking-in-space: NASA, 2017.

[3] J. Hsu, "Boeing and SpaceX Test the next U.S. Ride to Space: The International ...," *IEEE Spectrum*, Vol. 55, 2018, pp. 6–8, 10.1109/MSPEC.2018.8423570.

[4] E. Berger, *NASA Officials Outline Plans for Building a Lunar Gateway in the Mid-2020s*. Available: https://arstechnica.com/science/2020/03/nasa-officials-outline-plans-for-building-a-lunar-gateway-in-the-mid-2020s: Ars Technica, 2020.

[5] C. Gebhardt, *Mission Extension Vehicles succeed as Northrop Grumman works on future servicing/debris clean-up craft*. Available: https://www.nasaspaceflight.com/2021/05/mev-success-ng-future-servicing/: NASASpaceFlight, 2021.

[6] S. Clark, *Satellite in-space servicing demo mission a success*. Available: https://spaceflightnow.com/news/n0707/23oe/: Spaceflight Now, 2007.

[7] M. Vavrina, C. Skelton, K. Deweese, B. Naasz, D. Gaylor, and C. D'Souza, "Safe Rendezvous Trajectory Design for the Restore-L Mission," *Advances in the Astronautical Sciences*, Vol. 168, 2019, pp. 3649–3668.

[8] B. J. Naasz, "Safety Ellipse Motion With Coarse Sun Angle Optimization," *595 Flight Mechanics Symposium*, 2005.

[9] S. D'Amico, *Autonomous Formation Flying in Low Earth Orbit*. Delft, Netherlands: Ph.D. Thesis, TU Delft, 2010.

[10] O. Montenbruck, M. Kirschner, S. D'Amico, and S. Bettadpur, "E/I-Vector Separation for Safe Switching of the GRACE Formation," *IEEE Spectrum*, 2006, 10.1016/j.ast.2006.04.001.

[11] M. Zink and e. al., "The Tandem-X Mission Concept," *2006 IEEE International Symposium on Geoscience and Remote Sensing*, 2006, 10.1109/igarss.2006.501.

[12] E. Gill, S. D'Amico, and O. Montenbruck, "Autonomous Formation Flying for the PRISMA Mission," *Journal of Spacecraft and Rockets*, Vol. 44, No. 3, 2007, 10.2514/1.23015.

[13] G. Borelli, G. Gaias, and C. Colombo, "Safety in Forced Motion Guidance for Proximity Operations Based on Relative Orbital Elements," *AAS/AIAA 33rd Space Flight Mechanics Meeting*, 2023.

[14] J. Sullivan, *Nonlinear Angles-Only Orbit Estimation for Autonomous Distributed Space Systems*. Stanford, CA: Ph.D. Thesis, Stanford University, 2020.

[15] R. Fitzgerald, "Polynomial Conic Intersection Test," 2023.

[16] *FreeFlyer Astrodynamics Software*. Available: https://ai-solutions.com/freeflyer-astrodynamic-software/: a.i. solutions, Inc.

[17] J. R. Wertz and R. A. Bell, "Autonomous rendezvous and docking technologies: status and prospects," *SPIE Defense + Commercial Sensing*, 2003.

[18] M. Chernick, *Optimal Impulsive Control of Spacecraft Relative Motion*. Stanford, CA: Ph.D. Thesis, Stanford University, 2021.

[19] J. Sullivan, S. Grimberg, and S. D'Amico, "Comprehensive Survey and Assessment of Spacecraft Relative Motion Dynamics Models," *Journal of Guidance, Control, and Dynamics*, Vol. 40, 2017, pp. 1837–1859, 10.2514/1.G002309.

[20] K. Liu, *Generalized Cohn's Theorem*. Available: https://arxiv.org/pdf/0712.0116.pdf: The University of British Columbia, 2007.

[21] *numpy.roots*. Available: https://numpy.org/doc/stable/reference/generated/numpy.roots.html: NumPy Documentation.

[22] L. Riggi and S. D'Amico, "Optimal Impulsive Closed-Form Control for Spacecraft Formation Flying and Rendezvous," *2016 American Control Conference (ACC)*, 2016, 10.1109/ACC.2016.7526587.